Science Advances

MAAAS

Supplementary Materials for

Battery-free and AI-enabled multiplexed sensor patches for wound monitoring

Xin Ting Zheng *et al.*

Corresponding author: Benjamin C.K. Tee, benjamin.tee@nus.edu.sg; Xiaodi Su, xd-su@imre.a-star.edu.sg

This PDF file includes:

Supplementary Text

Colorimetric uric acid (UA) sensor optimization

Substantial design considerations and sensor optimizations have been carried out for the UA sensor to achieve desired color stability, well-maintained enzyme activity, good retention of colorimetric sensing reagents, similar calibration performance in PBS buffer vs simulated wound fluid (SWF) and negligible false positive signals.

Firstly, the color stability of the paper based colorimetric UA sensor is fine-tuned by choosing the right pH of the sensing matrix made of 1wt% chitosan during sensor fabrication stage. We have observed that intense background color is developed at lower UA concentration for UA sensors fabricated with a chitosan matrix of pH 5.5, whereas at a matrix pH 7.5, the sensor color quickly fades after 5 min. Color change is well maintained when the UA sensor is fabricated with a chitosan matrix of pH 6.5 for at least 40 min (**fig. S9a**).

Secondly, enzymatic activity is one of the major concerns in designing our UA sensor. We have sought to maintain the uricase activity by dissolving the enzymes in a stabilizer medium. As shown in **fig. S9b**, the color change is well maintained for enzymes dissolved in stabilizer solution (StabilCoat® Immunoassay Stabilizer) as compared to enzymes dissolved in phosphate buffered saline (PBS) after 1-day storage at 4°C fridge. And stabilizer enhanced UA sensor strips can be stored at room temperature for at least one weeks without substantial decay in enzyme activity.

Thirdly, to achieve a distinct color gradient according to analyte concentration on wax printed cellulose paper, we tested three different filter papers from Whatman, namely filter paper Grade 1, 2 and 3 of different thickness and particle retention. It is obvious from **fig. S9c** that only UA sensor in wax wells printed on Grade 3 filter paper with a smaller particle retention of 6 μm and a thickness of 390 μm can retain the colorimetric sensor reagents well, giving distinct color gradient upon addition of increasing concentrations of UA.

Fourthly, we have also compared the calibration of the uric acid sensors in PBS buffer versus the SWF to ascertain that the color response is of similar quality (**fig. S9d**).

Lastly, we investigated the false positive color change for UA sensors, involving different enzyme substrates. In the previous experiments, 3,3',5,5'-Tetramethylbenzidine (TMB) has been used as the enzymatic substrate which will develop blue color upon UA addition. We observe that TMB substrates are not stable, and they gradually self-oxidize to develop light blue color, which will

give rise to false positive signals. To minimize this effect, we have tested a few other substrates, including 4-aminoantipyrine (4-AAP) and o-Phenylenediamine (oPD). We found that 4-AAP is able to give a similarly distinct color gradient within minutes, and it does not show any false positive color even after hours (**fig. S9e**).

With all four aspects carefully considered and optimized for UA sensor, a well-correlated linear calibration is obtained for UA concentration of up to 1 mM, which well covers the clinically relevant UA concentration range in wounds.

Simultaneous detections of the five markers on wax-printed sensor panel

We first tested the sensor panel by adding the target analytes dissolved in phosphate buffer saline (PBS) directly to individual detection zones and observed their respective color change (**fig. S10**). As we increase the temperature from 31 ⁰C to 32 ⁰C and 33 ⁰C, the color of zone 1 (CLC temperature sensor) changes from red/orange to green to dark blue. For trimethylamine (TMA), the original grey color of TMA sensor is gradually bleached to light grey and off-white as the TMA concentration increases to 300 ppm and 3000 ppm, respectively. As the pH increases from 6.45 to 7.45 and 8.41, the color of zone 3 changes from yellow to light orange then dark orange. The moisture sensor is capable of reversible sensing, so its color remains blue if we maintain it dry on top of a hotplate. For the Uric acid (UA) sensor, a light pink color develops with the addition of 40 μM of UA. As the UA concentration further increases to 200 μM and even further to 800 μM, the pink color intensity is increased.

Demonstration of sensor panel response to healthy and unhealthy status of simulated wound fluid under flow conditions

To further demonstrate the usefulness of our sensor patch in real-life, we have composed two simulated wound fluids, one representing the healthy wound and the other one representing the unhealthy wound. The simulated wound fluids were added to the front center port of the sensor panel and then the fluid flow as well as the color change were recorded at specific time intervals. The sensor panels are fully wet after 8 min and stable color changes are observed at individual detection zones at 15 min (**fig. S11**).

Explainability in Machine Learning Algorithm Development

Convolutional neural networks may learn features that are not relevant to the region of interest, which could potentially affect the overall accuracy and its reliability to real-world application. To avoid including non-relevant features, we employed image locally interpretable model-agnostic explanation (*65*) (imageLIME) to visually check and explain the classification decisions made by our own model. Results shown in **fig. S18** indicates the correct network focuses on the pH region as well as uric acid region.
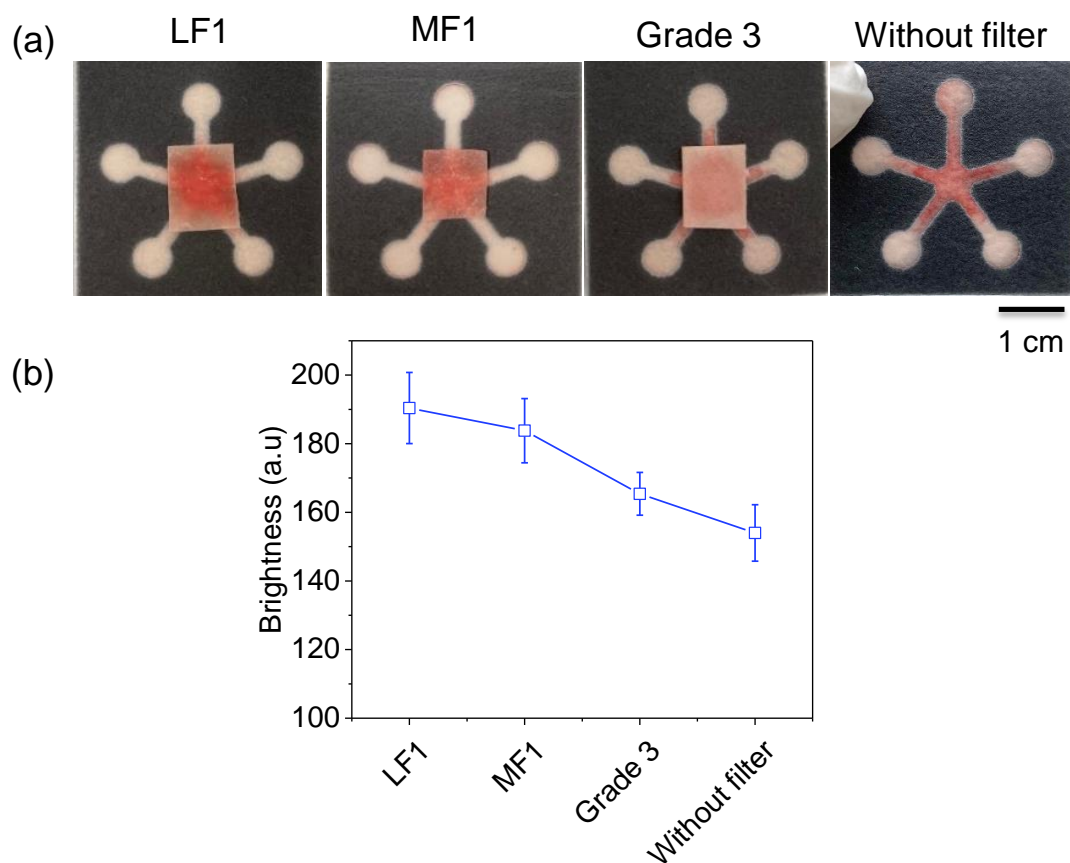
Fig. S1. Blood filtration membranes effectively reduce background color from blood. (a) Photos showing the effects of different blood filtration membranes (LF1 and MF1), filter paper (Whatman filter paper Grade 3) as compared to without filter after addition of sheep's whole blood. (b) The brightness values at the detection zones are in the order of LF1> MF1 >Grade 3 > without filter, indicating that LF1 is most effective in reducing background color from blood.
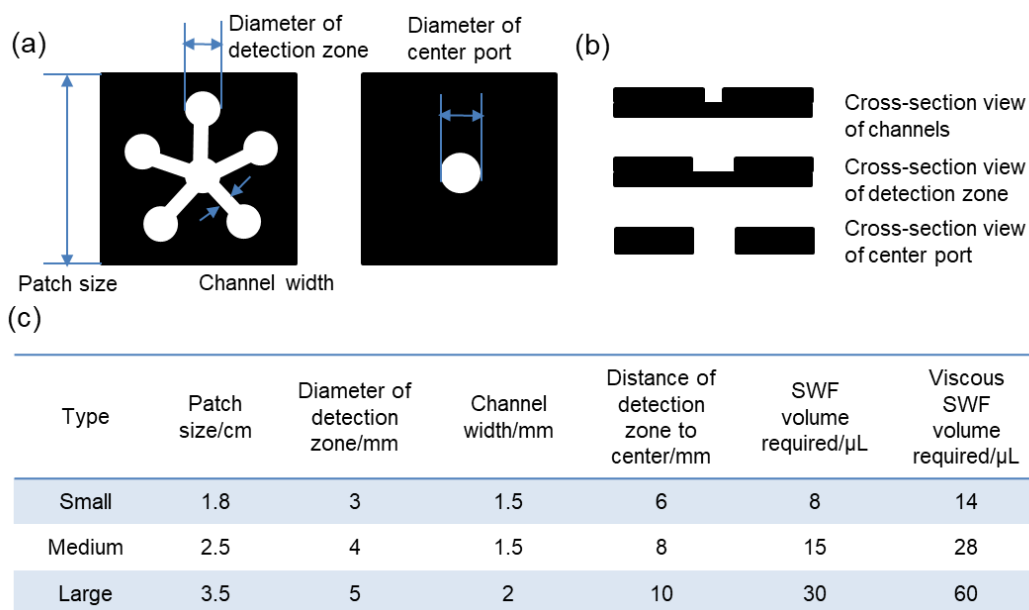
Type	Patch size/cm	Diameter of detection zone/mm	Channel width/mm	Distance of detection zone to center/mm	SWF volume required/μL	Viscous SWF volume required/μL
Small	1.8	3	1.5	6	8	14
Medium	2.5	4	1.5	8	15	28
Large	3.5	5	2	10	30	60

Fig. S2. Wax-printed panels with different sizes. (a) The design of the wax-printed panel. left: front view, right: back view; the wound exudate is expected to enter from the back center port, flows through the five channels and finally reaches the five detection zones; (b) cross-section view of the wax-printed panel at channel, detection zone and the center port. Black regions indicate wax impregnated paper that blocks fluid flow. The white regions indicate cellulose paper without wax, allowing fluid flow. (c) The dimensions of the wax-printed panel can be tailored to wound size, amount of wound exudate of low (~ 1 mPa·s) and high viscosity with 0.5 wt% xanthan gum (~ 80 mPa·s).
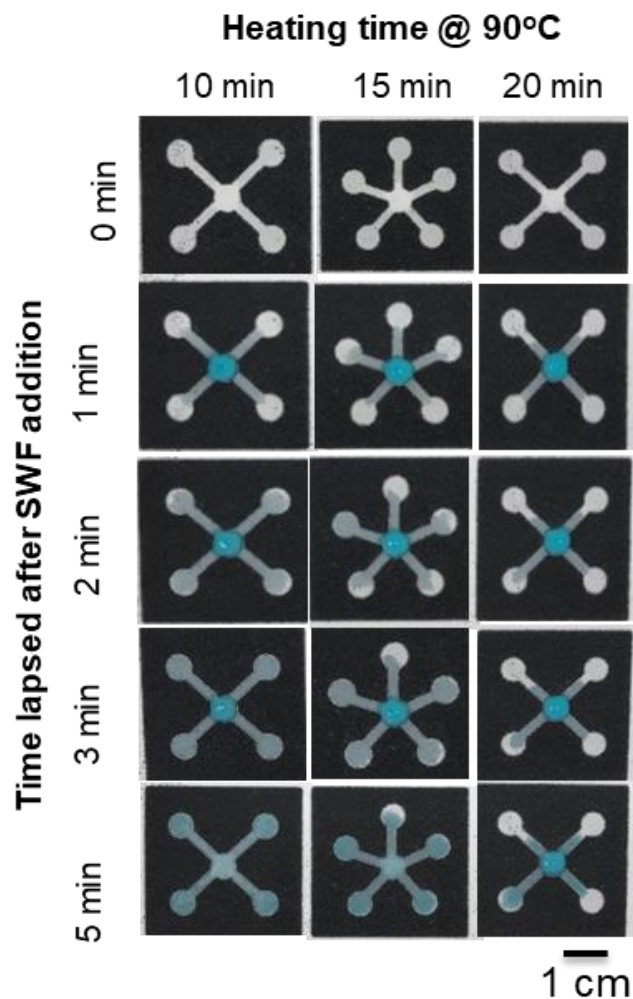
Fig. S3. The optimization of wax heating time. Wax heating time was optimized to fabricate channels with suitable channel depth for un-impeded flow of simulated wound fluid (SWF). The blue colored simulated wound fluid (SWF with $CuSO_4$ addition) were added to the center of each wax-printed panel to track the time taken for SWF to fully fill all five detection zones. An optimized heating time of 10 min at 90°C gives the shortest time (2-3 min) to fill all five detection zones.
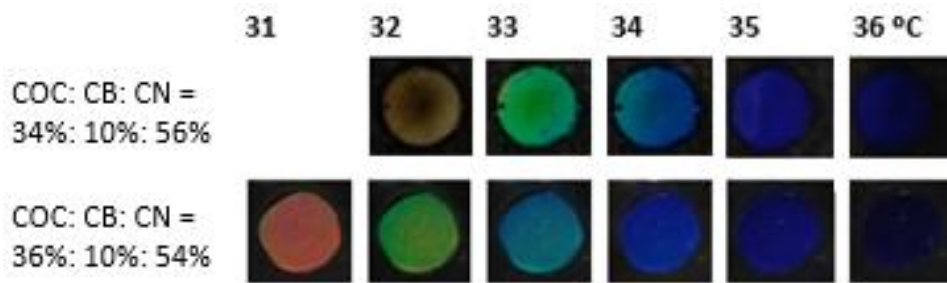
Fig. S4. Cholesteric liquid crystal (CLC) composition determines temperature range. Fine adjustments of the percentages of the three CLC components lead to different detectable temperature ranges.
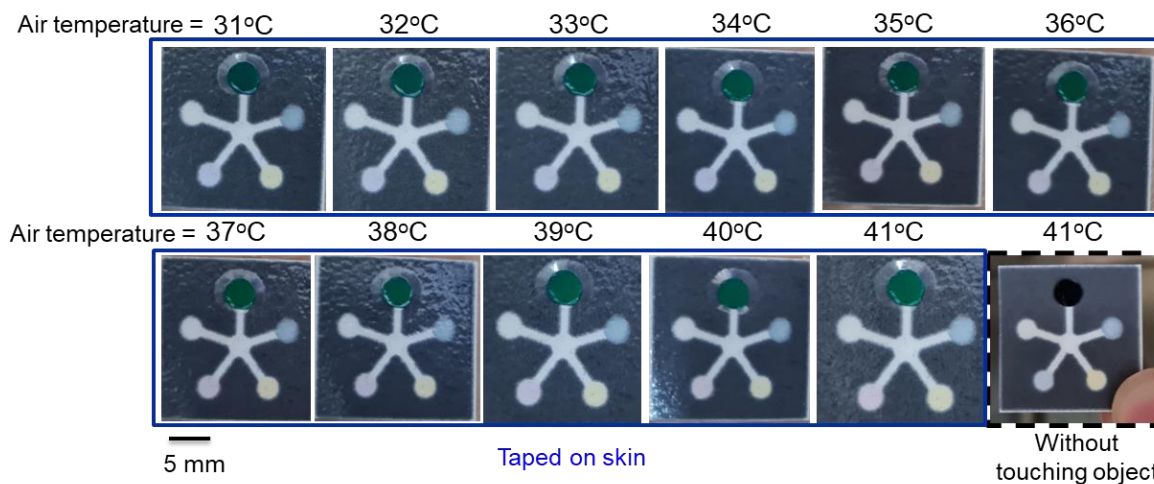

Fig. S5. The effect of ambient air temperature on CLC temperature sensor. When the CLC sensor was taped on skin with 32°C skin temperature (photos in blue box), it displayed the skin temperature (green color) but do not respond to the ambient temperature as it was increased from 31°C to 41°C. When the CLC sensor was put into an oven of 41°C without touching any object (photo in black dashed box), the CLC can sense the elevated temperature in the oven but eventually turned to black color because the temperature of 41°C was beyond its dynamic range of 31-36°C.
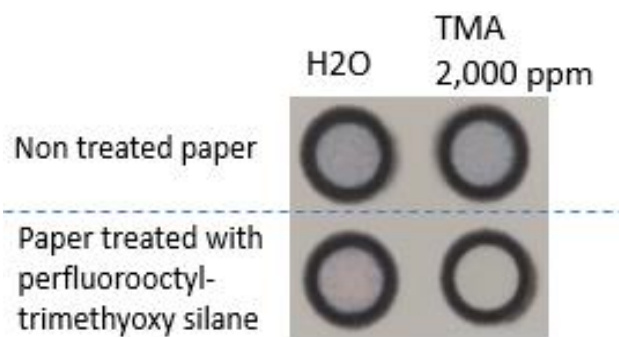
Fig. S6. Effect of perfluorooctyltrimethoxysilane treatment on TMA sensor outcome. The Reichardt's dye deposited on perfluorooctyltrimethoxysilane treated paper shows more distinct color response to TMA than that on non-treated paper.
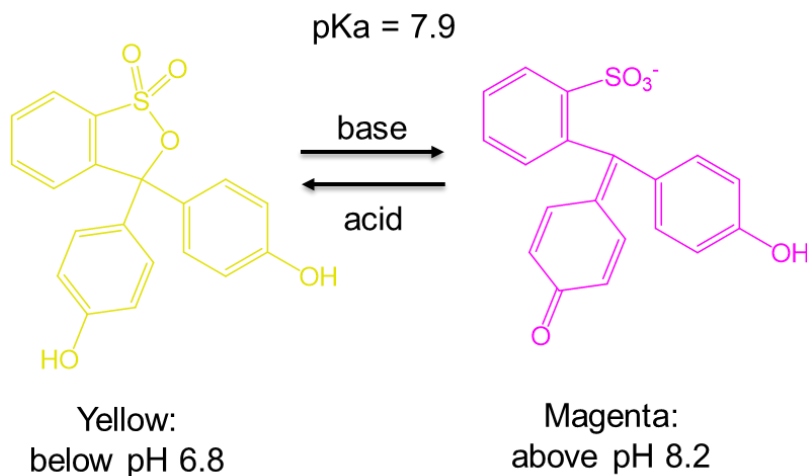

Fig. S7. The molecular structure of phenol red and its color change in response to pH. This dye shows yellow color below pH 6.8 and changes to magenta color above pH 8.2, which is suitable for detecting wound pH change.

Uricase

$$\text{Uric acid} + O_2 + H_2O \rightarrow \text{5-hydroxyisourate} + H_2O_2 \tag{1}$$

Horseradish Peroxidase

$$\text{Chromogenic substrate} + H_2O_2 \rightarrow \text{Colored product} + H_2O \tag{2}$$

Fig. S8. Colorimetric sensing of uric acid using uricase-peroxidase cascade reactions. Equation (1) shows the first step reaction whereby uricase catalyzes uric acid conversion and generates H_2O_2 as a by-product, and equation (2) shows the second step that horseradish peroxidase converts the chromogenic substrate (such as the 4-AAP) to a dark pink colored product in the presence of as-formed H_2O_2.
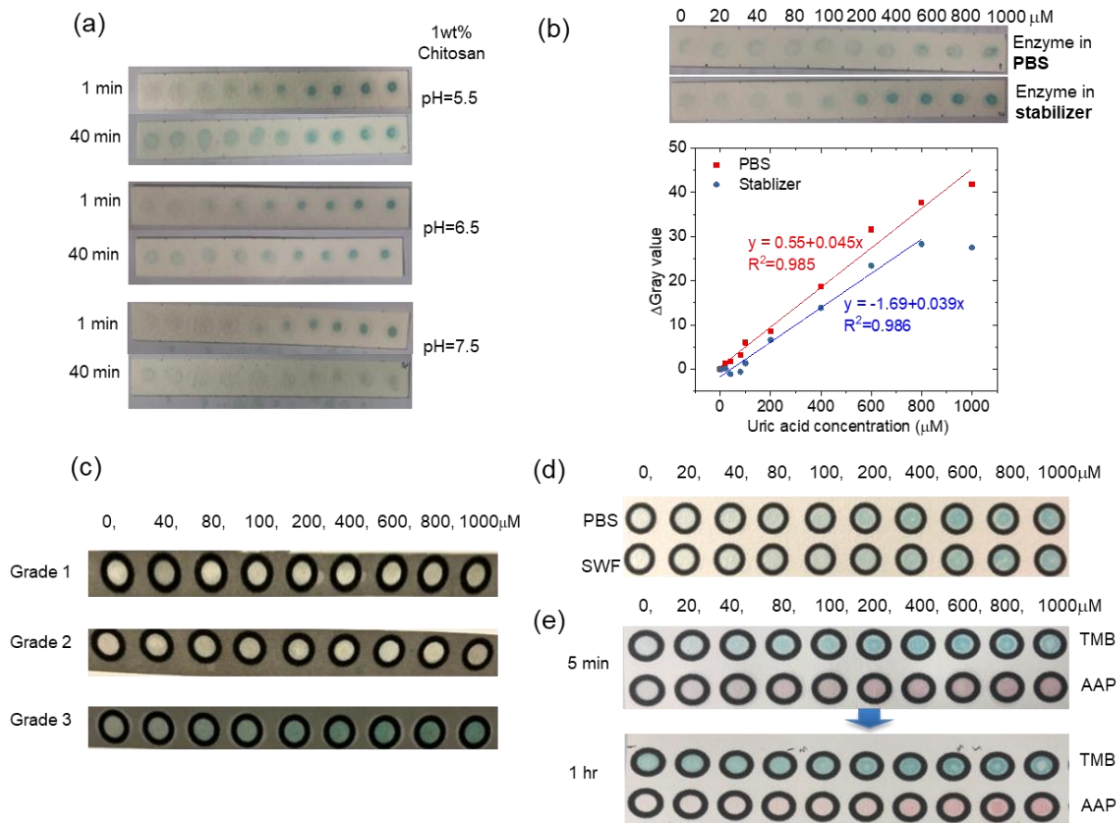

Fig. S9. Optimization of uric acid sensor. (a) The tuning of the chitosan sensing matrix pH for achieving color stability; (b) Comparison of the enzymatic activity for enzymes dissolved in PBS vs. stabilizer solution; (c) Comparison of color gradient development for UA sensor loaded in wax printed wells on different Whatman filter papers; (d) Comparison of UA sensor response in PBS vs. SWF; (e) Comparison of the false positive signals for TMB vs. AAP based UA sensor.
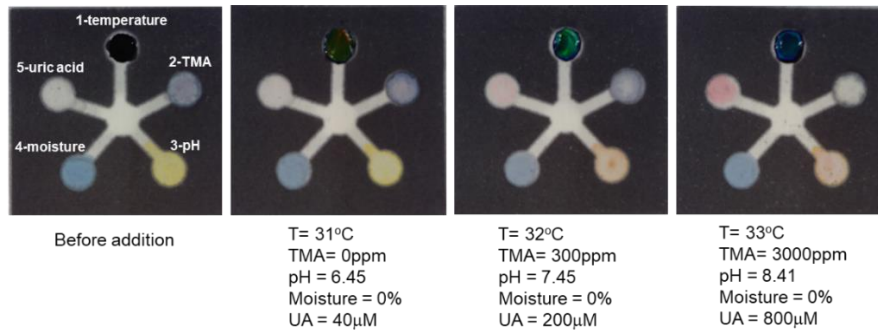
Fig. S10. Testing of potential crosstalk between different detection zones. When mixtures of the analytes (as specified in the list below the photos) were added to PETAL sensor patches, individual sensor shows specific color change to its intended target analyte indicating no interference between different sensors.
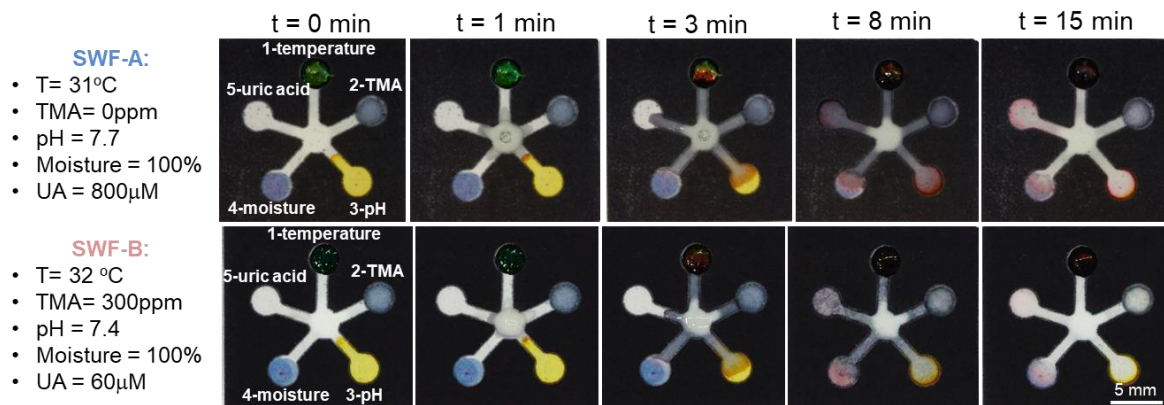

Fig. S11. Photos showing color development speed. The color development of the five sensors over time upon addition of two simulated wound fluids (SWF-A and SWF-B) to the center ports shows that all sensors are fully filled with SWF at 8 min and then fully reacted at 15 min.
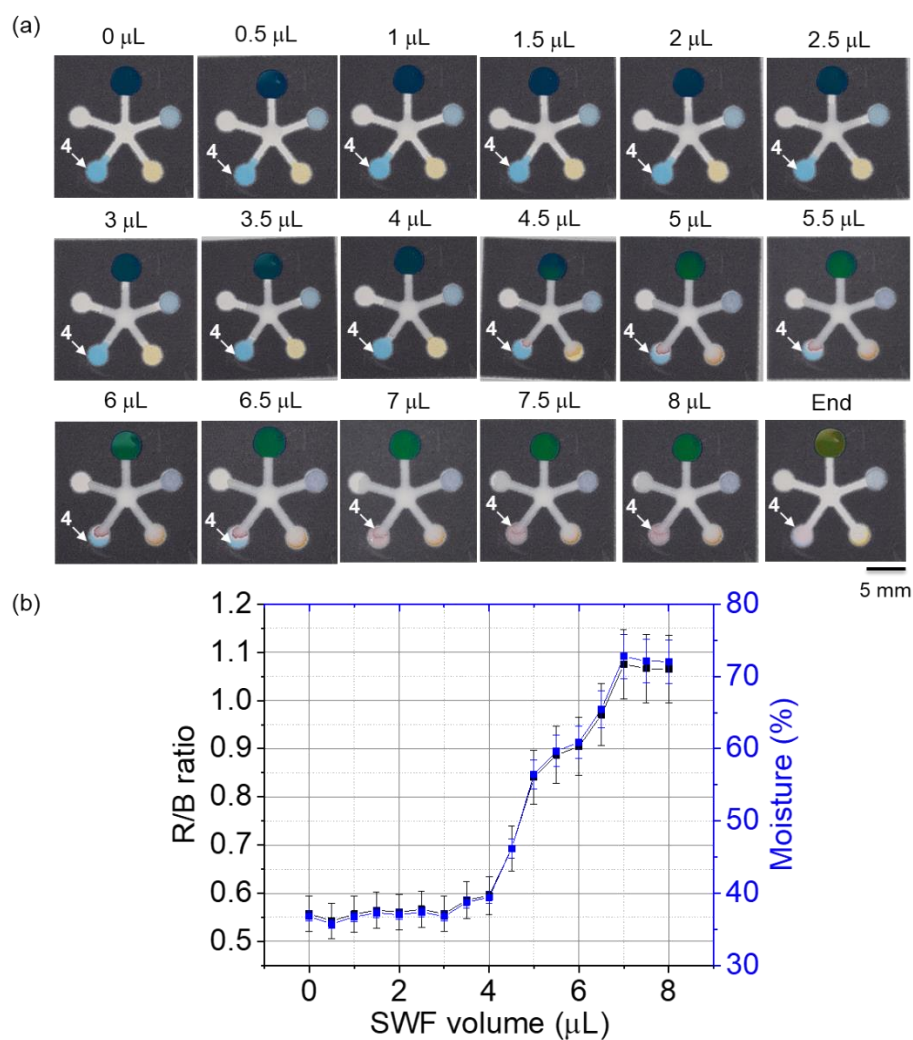
Fig. S12. The activation of moisture sensor at the 4th position of PETAL patch. (a) Gradual color change of moisture sensor upon dropwise SWF addition (0.5 μL/drop) up to 8 μL; (b) The change of R/B ratio and moisture % with respect to the total volume of SWF added.
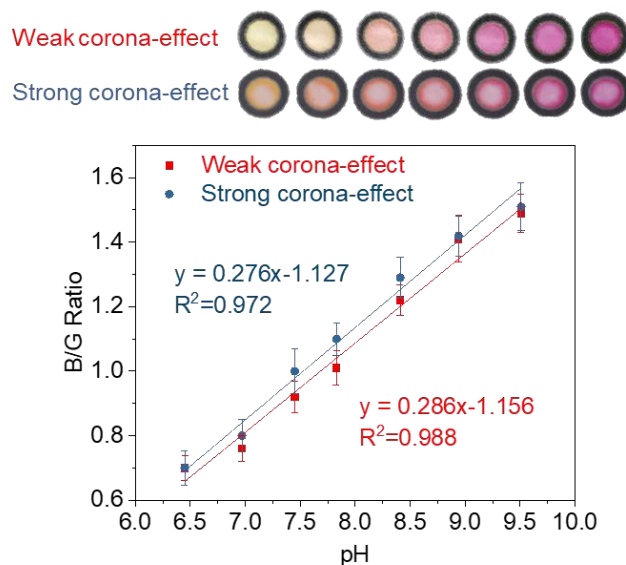
Fig. S13. The impact of corona-effect on colorimetric signal analysis. The plots show B/G ratios for pH sensor calibrations from the sensors with different extent of corona-effects. These two sets of pH sensors in wax-printed wells with different degrees of coffee ring effects were created by adjusting the liquid addition speeds.
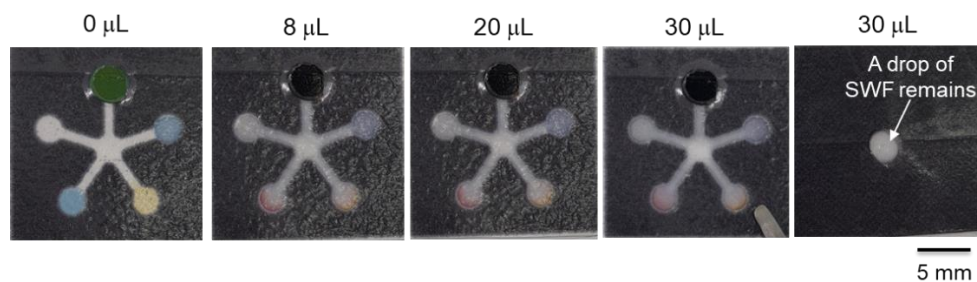
Fig. S14. Fluid uptake capacity of the small PETAL patch and the impact on color retention. The PETAL patch (1.8 cm) can absorb ~ 20 μL of SWF before it overflows, thereafter as 10 μL more SWF was added, a drop of SWF formed at the bottom inlet. No color leaching or reagents backflow towards the channel was observed for all cases.
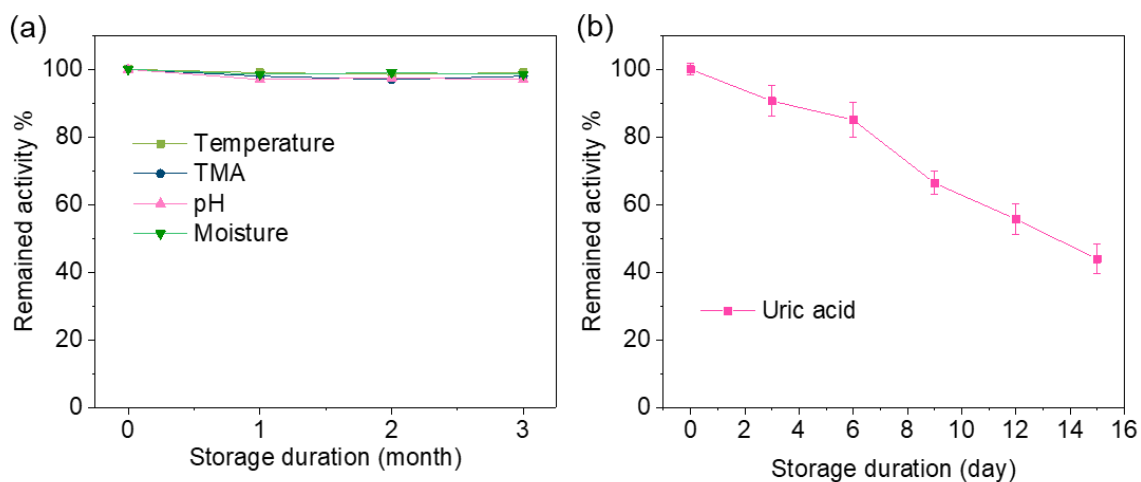

Fig. S15. Storage stability of five colorimetric sensors. Remained activity percentage of (a) temperature, TMA, pH, moisture sensors, and (b) uric acid sensor after a specified storage duration at room temperature.

Fig. S16. Training accuracy and loss of convolutional neural network for the perturbed wound model. Results show a high training accuracy of ~ 99% with very low training loss (difference between prediction and actual label).

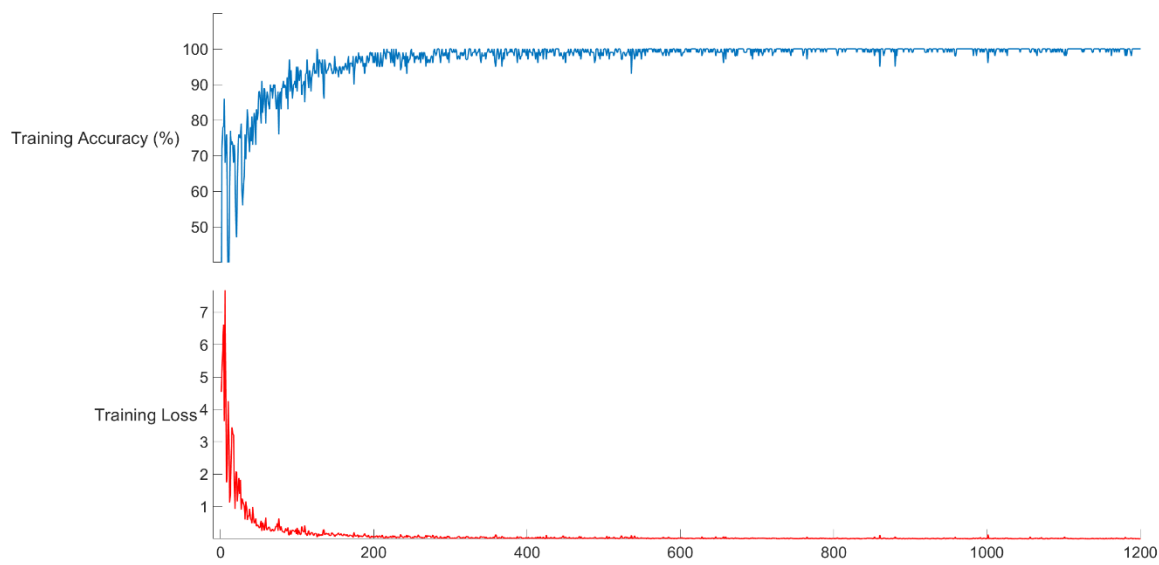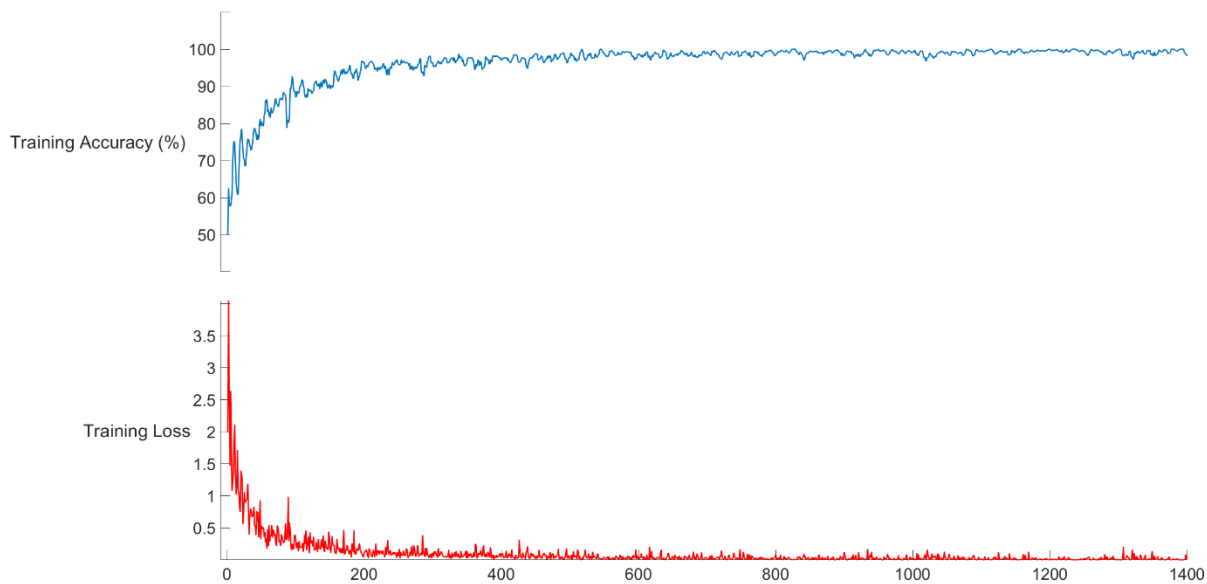**Fig. S17. Training accuracy and loss of convolutional neural network for the burn wound model.** Results show a high training accuracy of ~ 99% with very low training loss (difference between prediction and actual label).
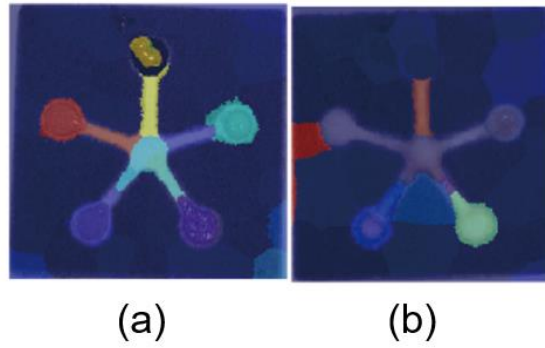
Fig. S18. Image LIME output image from perturb convolutional neural network. (a) Model A: Region in red color shows network predominantly focuses on the UA node. (b) Model B: Region in red color shows predominantly focuses on the black wax region, indicating Model B is ineffective.
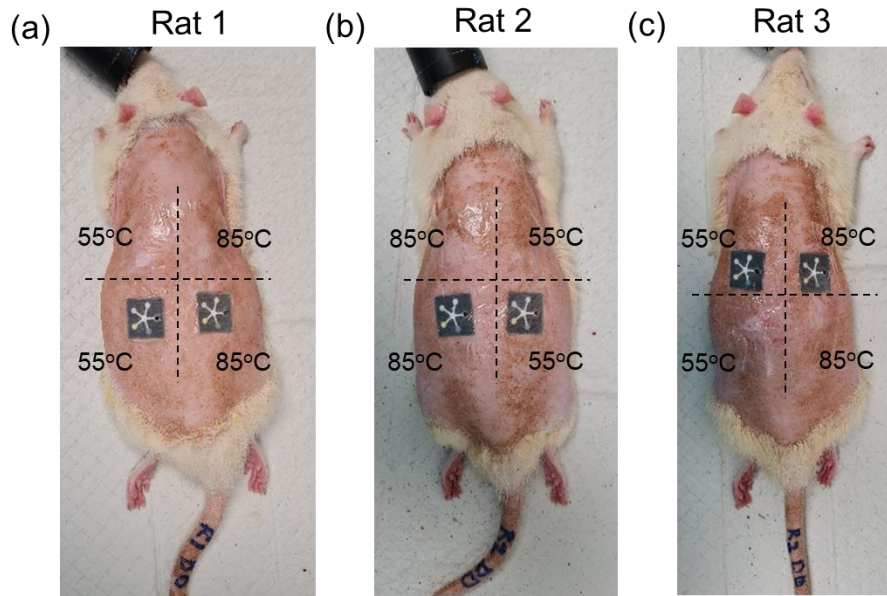
Fig. S19. PETAL sensor arrangement on each rat with four burn wounds. Photos showing the positions of burn wounds created and placements of PETAL sensor patches for (a) Rat 1, (b) Rat 2 and (c) Rat 3.
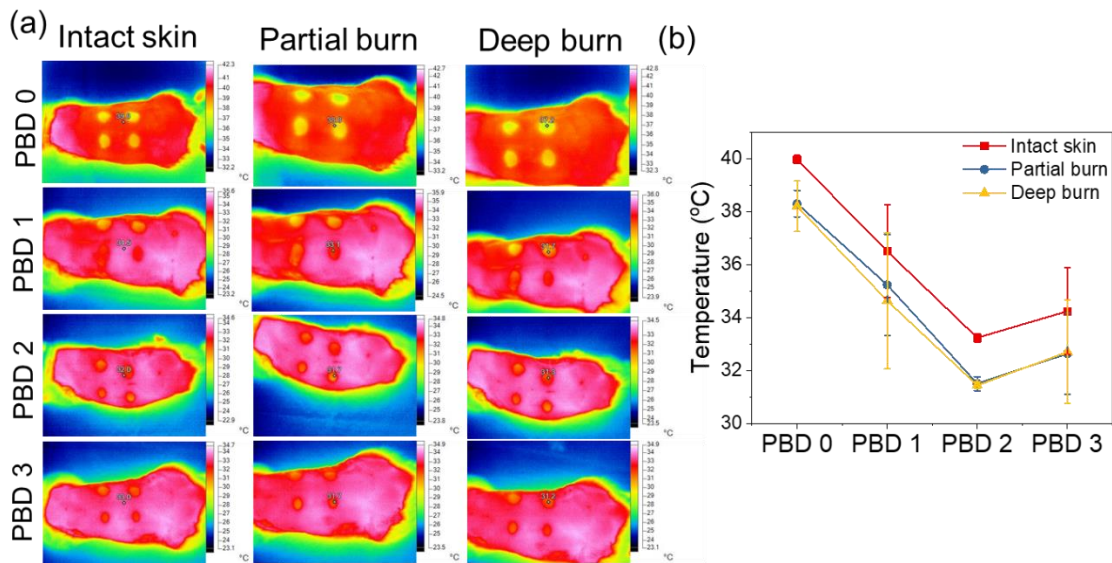
Fig. S20. The trend of temperature change after burn creation in rat model measured by Infrared camera. (a) Infra-red thermal images of rats taken on PBD 0 to PBD 3; (b) Temperature change for intact skin, partial burn and deep burn over the 4 days.
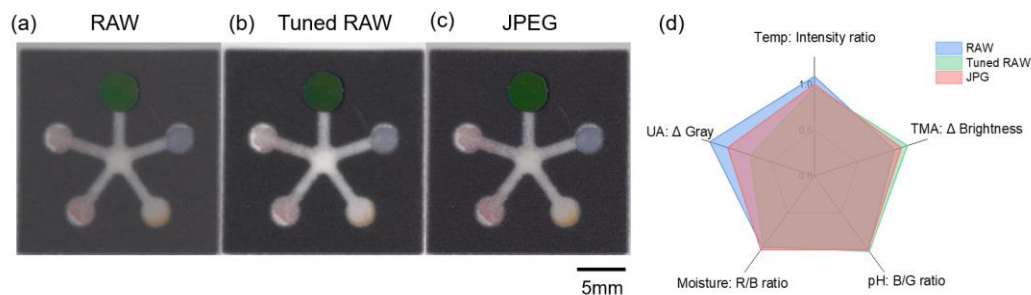
Fig. S21. Images with different processing methods. (a) With native function raw2rgb in Image processing toolbox. (b) with pipeline from Mathworks. (c) JPEG from smartphone. (d) radar plot of 3 format relative to JPEG. Results show that without carefully tuning pipeline parameter and use off-the-shelf raw2rgb function from MATLAB can lead to a deteriorated image quality compared to JPEG. After applying a complete processing pipeline, tuned RAW shows a similar color profile with JPEG. Therefore, JPEG is appropriate in our image analysis.
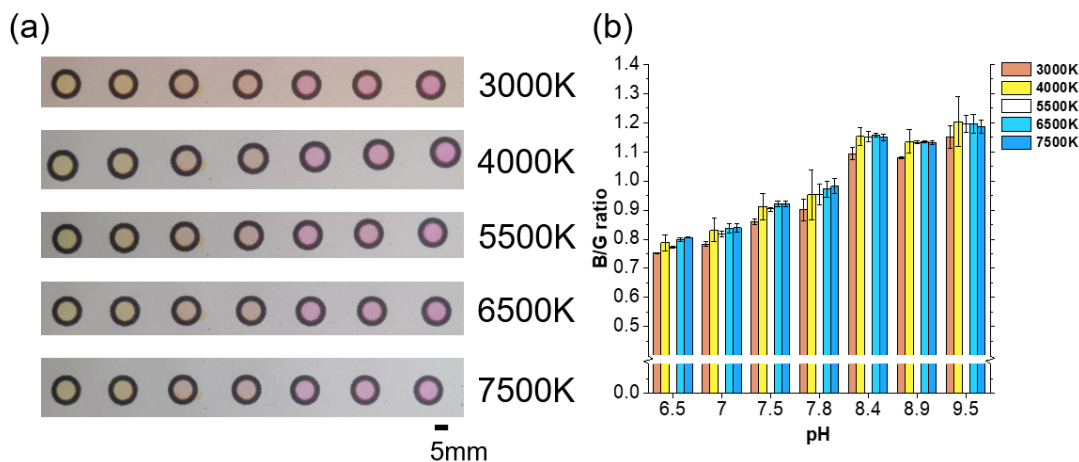
Fig. S22. **The effect of ambient light intensity on pH sensor signal.** (a) The images of the pH sensors under increasing light intensity. (b) B/G ratio of pH sensor under various light sources.
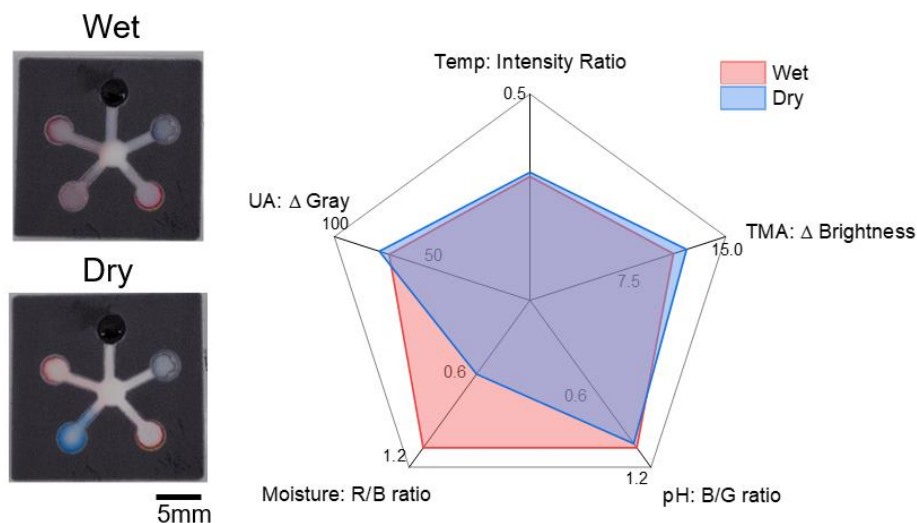
Fig. S23. Measured intensity or RGB ratio for each sensor node under wet and dry condition at ~ 15 min. Radar plot indicates negligible differences in feature values extracted from images taken under wet and dry conditions for all nodes except moisture.
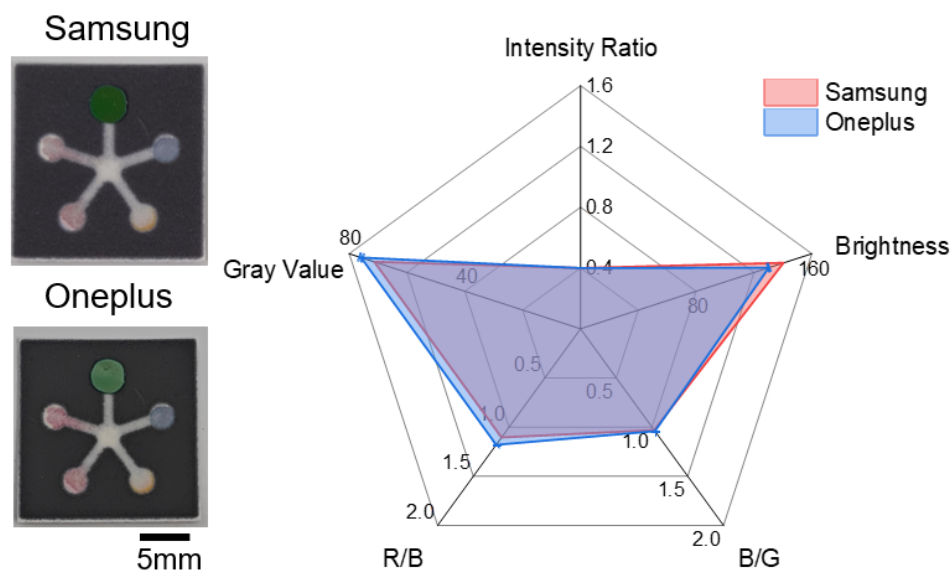
Fig. S24. Feature values collected from two different mobile phones. Images of PETAL sensors were captured with Oneplus 11 (IMX890 image sensor from Sony) and SAMSUNG Galaxy Note 20 (IMX555 from Sony) under the same condition.
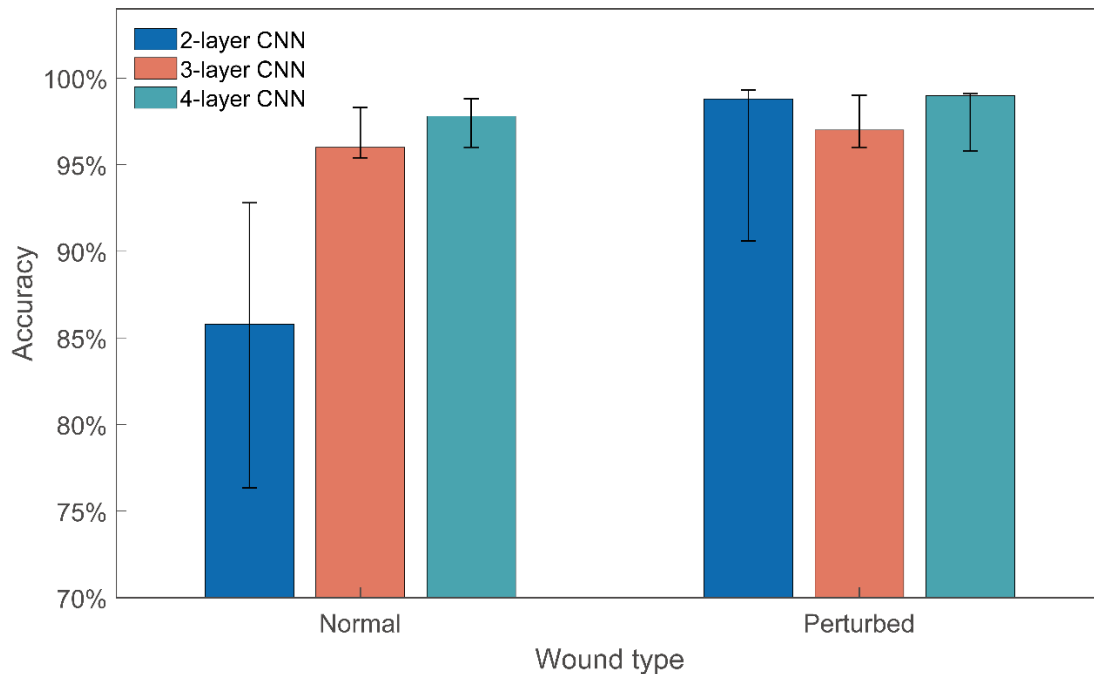
Fig. S25. Ablation study with different convolution layers. The graph shows high validation accuracy fluctuation for a 2-layer CNN, also the lowest accuracy level (for the normal wound). The accuracy of the 4-layer CNN is only slightly better than that of the 3 layers CNN (for both normal and perturbed wound classifications). Thus a 3-layer CNN is more robust in this scenario. Error bars refer to maximum and minimum deviation during training process (number of iterations, n = 100).

Table S1. The clinical significance of the five selected biomarkers and wound indicators in acute or chronic wounds.

No.	Wound marker	Clinical significance	Acute wound	Chronic wound
1	Temperature	Wound infection and delayed healing.(*30, 31*)	31-35 °C(*30, 31*)	1 °C increase relative to normal baseline level (*30*)
2	Trimethylamine (TMA)	Trimethylamine is a metabolite produced by most bacteria in wound.(*36*)	Not detected.	30-300 ppm(*37*)
3	pH	Increased wound pH as an indicator of local wound infection or unhealed wound.(*33*)	pH 6-8 with a mean of pH 6.7(*33*)	pH 6-9.5 with a mean of pH 8.1(*33*)
4	Moisture	Wound moisture levels are critical to healing.(*4*)	Varies by wound dressing(*35*)	A reference to indicate that sufficient wound exudate
5	Uric acid	A generic indicator for bacterial colonization or prolonged wound inflammation.(*4, 10*)	221 μM-751 μM range with a 347 μM median value(*46*)	50-100% relative decrease with respect the baseline level for prolonged inflammation or bacterial infection(*10*)·(*38*)

Table S2. The clinical significance of the five selected biomarkers and wound indicators in burn wounds.

No.	Wound marker	Clinical significance	Less severe burn	More severe burn
1	Temperature	Body temperature increases to maintain hypermetabolic process after burn	36-39 ^{o}C	(hyperthermia) ~40 °C or (hypothermia) ~35 °C(*32*)
2	Trimethylamine	Wound infection	Not detected or low conc.	Elevated conc. 30-300 ppm(*37*)
3	pH	Burn wound healing	Alkaline but reduces to acidic from day 5	Alkaline and takes longer to reduces to acidic(*34*)
4	Moisture	Wound moisture levels are critical to healing.	Varies by wound dressing type	A reference to indicate sufficient wound exudate
5	Uric acid	Elevated serum uric acid after injury correlates with the early acute kidney injury (AKI) in severe burns.	Low level	Elevated level(*39*)

REFERENCES AND NOTES

1. J. S. Chin, L. Madden, S. Y. Chew, D. L. Becker, Drug therapies and delivery mechanisms to treat perturbed skin wound healing. *Adv. Drug Deliv. Rev.* **149-150**, 2–18 (2019).

2. Y. Wang, M. Guo, B. He, B. Gao, Intelligent patches for wound management: In situ sensing and treatment. *Anal. Chem.* **93**, 4687–4696 (2021).

3. M. Ruiz-Castilla, O. Roca, J. R. Masclans, J. P. Barret, Recent advances in biomarkers in severe burns. *Shock* **45**, 117–125 (2016).

4. T. R. Dargaville, B. L. Farrugia, J. A. Broadbent, S. Pace, Z. Upton, N. H. Voelcker, Sensors and imaging for wound healing: A review. *Biosens. Bioelectron.* **41**, 30–42 (2013).

5. D. Church, S. Elsayed, O. Reid, B. Winston, R. Lindsay, Burn wound infections. *Clin. Microbiol. Rev.* **19**, 403–434 (2006).

6. A. Mischnik, M. Mieth, C. J. Busch, S. Hofer, S. Zimmermann, First evaluation of automated specimen inoculation for wound swab samples by use of the Previ Isola system compared to manual inoculation in a routine laboratory: Finding a cost-effective and accurate approach. *J. Clin. Microbiol.* **50**, 2732–2736 (2012).

7. D. M. Anisuzzaman, C. Wang, B. Rostami, S. Gopalakrishnan, J. Niezgoda, Z. Yu, Image-based artificial intelligence in wound assessment: A systematic review. *Adv. Wound Care* **11**, 687–709 (2022).

8. D. Lou, Q. Pang, X. Pei, S. Dong, S. Li, W.-q. Tan, L. Ma, Flexible wound healing system for pro-regeneration, temperature monitoring and infection early warning. *Biosens. Bioelectron.* **162**, 112275 (2020).

9. B. Qiao, Q. Pang, P. Yuan, Y. Luo, L. Ma, Smart wound dressing for infection monitoring and NIR-triggered antibacterial treatment. *Biomater. Sci.* **8**, 1649–1657 (2020).

10. P. Kassal, J. Kim, R. Kumar, W. R. de Araujo, I. M. Steinberg, M. D. Steinberg, J. Wang, Smart bandage with wireless connectivity for uric acid biosensing as an indicator of wound status. *Electrochem. Commun.* **56**, 6–10 (2015).

11. Z. Xiong, S. Achavananthadith, S. Lian, L. E. Madden, Z. X. Ong, W. Chua, V. Kalidasan, Z. Li, Z. Liu, P. Singh, H. Yang, S. P. Heussler, S. M. P. Kalaiselvi, M. B. H. Breese, H. Yao, Y. Gao, K. Sanmugam, B. C. K. Tee, P. Y. Chen, W. Loke, C. T. Lim, G. S. H. Chiang, B. Y. Tan, H. Li, D. L. Becker, J. S. Ho, A wireless and battery-free wound infection sensor based on DNA hydrogel. *Sci. Adv.* **7**, eabj1617 (2021).

12. S. Kalasin, P. Sangnuang, W. Surareungchai, Intelligent wearable sensors interconnected with advanced wound dressing bandages for contactless chronic skin monitoring: Artificial intelligence for predicting tissue regeneration. *Anal. Chem.* **94**, 6842–6852 (2022).

13. S. Shrivastava, T. Q. Trung, N.-E. Lee, Recent progress, challenges, and prospects of fully integrated mobile and wearable point-of-care testing systems for self-testing. *Chem. Soc. Rev.* **49**, 1812–1866 (2020).

14. S. Bauer, Sophisticated skin. *Nat. Mater.* **12**, 871–872 (2013).

15. D.-H. Kim, N. Lu, R. Ma, Y.-S. Kim, R.-H. Kim, S. Wang, J. Wu, S. M. Won, H. Tao, A. Islam, K. J. Yu, T.-i. Kim, R. Chowdhury, M. Ying, L. Xu, M. Li, H.-J. Chung, H. Keum, M. McCormick, P. Liu, Y.-W. Zhang, F. G. Omenetto, Y. Huang, T. Coleman, J. A. Rogers, Epidermal electronics. *Science* **333**, 838–843 (2011).

16. J. A. Rogers, T. Someya, Y. Huang, Materials and mechanics for stretchable electronics. *Science* **327**, 1603–1607 (2010).

17. B. C. K. Tee, J. Ouyang, Soft electronically functional polymeric composite materials for a flexible and stretchable digital future. *Adv. Mater.* **30**, 1802560 (2018).

18. Y. Zhao, A. Kim, G. Wan, B. C. K. Tee, Design and applications of stretchable and self-healable conductors for soft electronics. *Nano Converg.* **6**, 25 (2019).

19. T. Djenizian, B. C. K. Tee, M. Ramuz, L. Fang, Advances in flexible and soft electronics. *APL Materials* **7**, 031201 (2019).

20. Q. Pang, D. Lou, S. Li, G. Wang, B. Qiao, S. Dong, L. Ma, C. Gao, Z. Wu, Smart flexible electronics-integrated wound dressing for real-time monitoring and on-demand treatment of infected wounds. *Adv. Sci.* **7**, 1902673 (2020).

21. B. K. Ashley, M. S. Brown, Y. Park, S. Kuan, A. Koh, Skin-inspired, open mesh electrochemical sensors for lactate and oxygen monitoring. *Biosens. Bioelectron.* **132**, 343–351 (2019).

22. C. Wang, E. Shirzaei Sani, W. Gao, Wearable bioelectronics for chronic wound management. *Adv. Funct. Mater.* **32**, 2111022 (2022).

23. P. Mostafalu, A. Tamayol, R. Rahimi, M. Ochoa, A. Khalilpour, G. Kiaee, I. K. Yazdi, S. Bagherifard, M. R. Dokmeci, B. Ziaie, S. R. Sonkusale, A. Khademhosseini, Smart bandage for monitoring and treatment of chronic wounds. *Small* **14**, 1703509 (2018).

24. Y. Gao, D. T. Nguyen, T. Yeo, S. B. Lim, W. X. Tan, L. E. Madden, L. Jin, J. Y. K. Long, F. A. B. Aloweni, Y. J. A. Liew, M. L. L. Tan, S. Y. Ang, S. D. O. Maniya, I. Abdelwahab, K. P. Loh, C.-H. Chen, D. L. Becker, D. Leavesley, J. S. Ho, C. T. Lim, A flexible multiplexed immunosensor for point-of-care in situ wound monitoring. *Sci. Adv.* **7**, eabg9614 (2021).

25. S. RoyChoudhury, Y. Umasankar, J. Jaller, I. Herskovitz, J. Mervis, E. Darwin, P. A. Hirt, L. J. Borda, H. A. Lev-Tov, R. Kirsner, S. Bhansali, Continuous monitoring of wound healing using a wearable enzymatic uric acid biosensor. *J. Electrochem. Soc.* **165**, B3168–B3175 (2018).

26. J. T. Connelly, J. P. Rolland, G. M. Whitesides, "Paper machine" for molecular diagnostics. *Anal. Chem.* **87**, 7595–7601 (2015).

27. M. S. Verma, M. N. Tsaloglou, T. Sisley, D. Christodouleas, A. Chen, J. Milette, G. M. Whitesides, Sliding-strip microfluidic device enables ELISA on paper. *Biosens. Bioelectron.* **99**, 77–84 (2018).

28. E. Carrilho, A. W. Martinez, G. M. Whitesides, Understanding wax printing: A simple micropatterning process for paper-based microfluidics. *Anal. Chem.* **81**, 7091–7095 (2009).

29. Y. Zhu, J. Zhang, J. Song, J. Yang, Z. Du, W. Zhao, H. Guo, C. Wen, Q. Li, X. Sui, L. Zhang, A multifunctional pro-healing zwitterionic hydrogel for simultaneous optical monitoring of pH and glucose in diabetic wound treatment. *Adv. Funct. Mater.* **30**, 1905493 (2020).

30. M. S. Brown, B. Ashley, A. Koh, Wearable technology for chronic wound monitoring: Current dressings, advancements, and future prospects. *Front. Bioeng. Biotechnol.* **6**, 47 (2018).

31. V. Dini, P. Salvo, A. Janowska, F. D. Francesco, A. Barbini, M. Romanelli, Correlation between wound temperature obtained with an infrared camera and clinical wound bed score in venous leg ulcers. *Wounds* **27**, 274–278 (2015).

32. J. Bayuo, Management strategies of burns associated hyperthermia: A case report. *Burns Open* **1**, 45–47 (2017).

33. S. Ono, R. Imai, Y. Ida, D. Shibata, T. Komiya, H. Matsumura, Increased wound pH as an indicator of local wound infection in second degree burns. *Burns* **41**, 820–824 (2015).

34. E. Osti, Skin ph variations from the acute phase to re-epithelialization in burn patients treated with new materials (burnshield, semipermeable adhesive film, dermasilk, and hyalomatrix). Non-invasive preliminary experimental clinical trial. *Ann. Burns Fire Disasters* **21**, 73–77 (2008).

35. M. Ochoa, R. Rahimi, B. Ziaie, Flexible sensors for chronic wound management. *IEEE Rev. Biomed. Eng.* **7**, 73–86 (2014).

36. L. D. J. Bos, P. J. Sterk, M. J. Schultz, Volatile metabolites of pathogens: A systematic review. *PLOS Pathog.* **9**, e1003311 (2013).

37. C. Salinas Alvarez, D. Sierra-Sosa, B. Garcia-Zapirain, D. Yoder-Himes, A. Elmaghraby, A detection of volatile compounds emitted by bacteria in wounds using gas sensors. *Sensors* **19**, 1523 (2019).

38. M. L. Fernandez, Z. Upton, H. Edwards, K. Finlayson, G. K. Shooter, Elevated uric acid correlates with wound severity. *Int. Wound J.* **9**, 139–149 (2012).

39. J. Liang, P. Zhang, X. Hu, L. Zhi, Elevated serum uric acid after injury correlates with the early acute kidney in severe burns. *Burns* **41**, 1724–1731 (2015).

40. C. Reichardt, Solvatochromic dyes as solvent polarity indicators. *Chem. Rev.* **94**, 2319–2358 (1994).

41. J. B. Essner, G. A. Baker, Ionic liquid inspired alkalinochromic salts based on Reichardt's dyes for the solution phase and vapochromic detection of amines. *Anal. Bioanal. Chem.* **410**, 4607–4613 (2018).

42. A. Koh, D. Kang, Y. Xue, S. Lee, R. M. Pielak, J. Kim, T. Hwang, S. Min, A. Banks, P. Bastien, M. C. Manco, L. Wang, K. R. Ammann, K.-I. Jang, P. Won, S. Han, R. Ghaffari, U. Paik, M. J. Slepian, G. Balooch, Y. Huang, J. A. Rogers, A soft, wearable microfluidic device for the capture, storage, and colorimetric sensing of sweat. *Sci. Transl. Med.* **8**, 366ra165 (2016).

43. X. Wang, F. Li, Z. Cai, K. Liu, J. Li, B. Zhang, J. He, Sensitive colorimetric assay for uric acid and glucose detection based on multilayer-modified paper with smartphone as signal readout. *Anal. Bioanal. Chem.* **410**, 2647–2655 (2018).

44. Y. Yang, E. Noviana, M. P. Nguyen, B. J. Geiss, D. S. Dandy, C. S. Henry, Paper-based microfluidic devices: Emerging themes and applications. *Anal. Chem.* **89**, 71–91 (2017).

45. C. Öhlknecht, G. Tegl, B. Beer, C. Sygmund, R. Ludwig, G. M. Guebitz, Cellobiose dehydrogenase and chitosan-based lysozyme responsive materials for antimicrobial wound treatment. *Biotechnol. Bioeng.* **114**, 416–422 (2017).

46. N. J. Trengove, S. R. Langton, M. C. Stacey, Biochemical analysis of wound fluid from nonhealing and healing chronic leg ulcers. *Wound Repair Regen.* **4**, 234–239 (1996).

47. R. Ghosh, V. Vaishampayan, A. Mahapatra, R. Malhotra, S. Balasubramanian, A. Kapoor, Enhancement of limit of detection by inducing coffee-ring effect in water quality monitoring microfluidic paper-based devices. *Desalin. Water Treat.* **156**, 316–322 (2019).

48. K. N. Al-Milaji, H. Zhao, New perspective of mitigating the coffee-ring effect: Interfacial assembly. *J. Phys. Chem. C* **123**, 12029–12041 (2019).

49. J. S. Chin, D. L. Becker, *World Union of Wound Healing Societies Congress*, Abu Dhabi, UAE, 1 to 5 March 2022.

50. R. M. Johnson, R. Richard, Partial-thickness burns: Identification and management. *Adv. Skin Wound Care* **16**, 178–187 (2003).

51. V. Singh, L. Devgan, S. Bhat, S. M. Milner, The pathogenesis of burn wound conversion. *Ann. Plast. Surg.* **59**, 109–115 (2007).

52. A. J. Singer, S. T. Boyce, Burn wound healing and tissue engineering. *J. Burn Care Res.* **38**, e605–e613 (2017).

53. D. M. Jackson, The diagnosis of the depth of burning. *Br. J. Surg.* **40**, 588–596 (1953).

54. L. O. Lamke, G. E. Nilsson, H. L. Reithner, The evaporative water loss from burns and the water-vapour permeability of grafts and artificial membranes used in the treatment of burns. *Burns* **3**, 159–165 (1977).

55. K. F. Cutting, R. J. White, Maceration of the skin and wound bed. 1: Its nature and causes. *J. Wound Care* **11**, 275–278 (2002).

56. B. Bates-Jensen, G. Schultz, L. G. Ovington, Management of exudate, biofilms, and infection, in *Wound Care: A Collaborative Practice Manual* (Wolters Kluwer, ed. 4, 2012), pp. 457–476.

57. P. Vowden, E. Bond, F. Meuleneire, Managing high viscosity exudate. *Wounds UK* **11**, 56–60 (2015).

58. W. Guo, J. Hansson, W. van der Wijngaart, Synthetic paper separates plasma from whole blood with low protein loss. *Anal. Chem.* **92**, 6194–6199 (2020).

59. R. A. Robinson, R. H. Stokes, *Electrolyte Solutions* (Butterworths, ed. 2, 1968).

60. K. Zhang, W. Zuo, Y. Chen, D. Meng, L. Zhang, Beyond a gaussian denoiser: Residual learning of deep cnn for image denoising. *IEEE Trans. Image Process.* **26**, 3142–3155 (2017).

61. K. Team, Simple MNIST convnet (2022); https://keras.io/examples/vision/mnist_convnet/.

62. L. Guo, T. Wang, Z. Wu, J. Wang, M. Wang, Z. Cui, S. Ji, J. Cai, C. Xu, X. Chen, Portable food-freshness prediction platform based on colorimetric barcode combinatorics and deep convolutional neural networks. *Adv. Mater.* **32**, 2004805 (2020).

63. Z. Lu, N. Lu, Y. Xiao, Y. Zhang, Z. Tang, M. Zhang, Metal-nanoparticle-supported nanozyme-based colorimetric sensor array for precise identification of proteins and oral bacteria. *ACS Appl. Mater. Interfaces* **14**, 11156–11166 (2022).

64. Z. Li, J. R. Askim, K. S. Suslick, The optoelectronic nose: Colorimetric and fluorometric sensor arrays. *Chem. Rev.* **119**, 231–292 (2019).

65. M. T. Ribeiro, S. Singh, C. Guestrin, "Why should I trust you?" Explaining the predictions of any classifier, in *Proceedings of the 22nd ACM SIGKDD International Conference on Knowledge Discovery and Data Mining* (Association for Computing Machinery, 2016), pp. 1135–1144.